Revision 1

Thermal and combined high-temperature and high-pressure behavior of a natural intermediate scapolite

Paolo Lotti[1]*, G. Diego Gatta[1], Lara Gigli[2], Hannes Krüger[3], Volker Kahlenberg[3], Martin Meven[4], Davide Comboni[1,5], Sula Milani[1], Marco Merlini[1], Hanns-Peter Liermann[6]

[1] Dipartimento di Scienze della Terra, Università degli Studi di Milano, Via Botticelli 23, 20133, Milano, Italy.

[2] Elettra Sincrotrone Trieste S.c.P.A., Strada Statale 14 – km 163.5 in AREA Science Park, 34149 Basovizza, Trieste, Italy.

[3] Institut für Mineralogie und Petrographie, Leopold-Franzens Universität Innsbruck, Innrain 52, 6020 Innsbruck, Austria.

[4] Institut für Kristallographie, RWTH Aachen, and Jülich Centre of Neutron Science at the Heinz Maier-Leibnitz Zentrum, Lichtenbergstraße 1, 85748 Garching, Germany

[5] European Synchrotron Radiation Facility, 71 Avenue des Martyrs, CS40220, 38043 Grenoble Cedex, France

[6] Photon Sciences, DESY, PETRA-III, Notkestrasse 85, 22607 Hamburg, Germany

* corresponding author: Paolo Lotti – paolo.lotti@unimi.it; Office Tel: +390250315601

Word counts: 9350

Abstract

A natural intermediate member of the scapolite solid solution (Me_{47}; experimental chemical formula: $(Na_{1.86}Ca_{1.86}K_{0.23}Fe_{0.01})(Al_{4.36}Si_{7.64})O_{24}[Cl_{0.48}(CO_3)_{0.48}(SO_4)_{0.01}]$), with the unusual *I*4/*m* space group, has been studied at various temperatures and combined high-*T* and high-*P* by means of *in situ* single-crystal and powder X-ray diffraction, at both conventional and synchrotron sources. In addition, single-crystal neutron diffraction data were collected at ambient-*T* and 685 °C. A fit of the experimental *V*-*T* data with a thermal equation of state yielded a calculated thermal expansion coefficient at ambient conditions: $\alpha_{V25°C} = 1/V_0 \cdot (\partial V/\partial T)_{P,25°C} = 1.74(3) \cdot 10^{-5}$ K^{-1}. A comparative analysis of the elastic behavior of scapolite based on this study and other high-*T* XRD data reported in the literature suggests that a thorough re-investigation of the different members of the marialite-meionite solid solution is needed to fully understand the role of crystal chemistry on the thermal behavior of these complex non-binary solid solutions. The experimental data obtained within the full temperature range of analysis at ambient pressure confirm that the investigated sample always preserves the *I*4/*m* space group, and possible implications on the metastability of *I*4/*m* intermediate scapolite are discussed. Neutron diffraction data show that no significant Si and Al re-arrangement among the *T* sites occurs between 25 and 685 °C. The combined high-*T* and high-*P* data show that at 650 °C and between 10.30(5) and 10.71(5) GPa a phase transition towards a triclinic polymorph occurs, with a positive Clapeyron slope (*i.e.*, d*P*/d*T* > 0). A comprehensive description of the atomic-scale structure deformation mechanisms induced by temperature and/or pressure, including those leading to structural instability, is provided based on single-crystal structure refinements.

Keywords: scapolite, temperature, pressure, phase transition, synchrotron data, neutron data

1. Introduction

Scapolites are a group of open-framework aluminosilicates with general formula $M_4T_{12}O_{24}A$, where M are monovalent or divalent cations (usually Na, Ca and minor K), T are trivalent or tetravalent cations (mostly Al and Si) in tetrahedral coordination, and A are anionic elements or groups as Cl, CO_3 and SO_4. Three mineral end-members are recognized: marialite, $Na_4Al_3Si_9O_{24}Cl$, meionite, $Ca_4Al_6Si_6O_{24}CO_3$, and silvialite, $Ca_4Al_6Si_6O_{24}SO_4$, even though most of the natural samples are of an intermediate composition (see *e.g.* Seto et al. 2004).

Scapolites represent a complex and non-binary solid solution, characterized, at a first approximation, by the NaSi ↔ CaAl and the NaCl ↔ $Ca(CO_3,SO_4)$ substitutions. Following the pioneering works of Shaw (1960a,b) and Evans et al. (1969), on the crystal chemistry of scapolite-group minerals, more recent studies (Zolotarev 1996; Teerstra and Sheriff 1997; Seto et al. 2004; Sokolova and Hawthorne 2008; Hawthorne and Sokolova 2008) revealed that natural scapolites follow three different compositional trends along the marialite-meionite joint, with discontinuities at 3.6 and 4.7 Al atoms per formula units (Teerstra and Sheriff 1997).

A common formalism, widely adopted to refer to a member of the scapolite solid solution, is that of meionite fraction (Shaw 1960a,b): $Me\% = (\sum M^{2+}/\sum M^{+} + M^{2+})\cdot 100$. Due to the complex nature of the chemical substitutions within the solid solution series, this formalism is not accurate, but can still be considered as valid at a first approximation (Sokolova and Hawthorne 2008) and will be adopted also throughout this manuscript.

Beside their complex chemical features, scapolites are also characterized by the presence of two crystal chemistry-controlled polymorphs: samples with a composition closer to the marialite and meionite end-members are usually reported to crystallize with a structure described in the $I4/m$ space group, whereas intermediate members are reported to show a $P4_2/n$ symmetry. A detailed

discussion on the crystal chemical and structural reasons for the occurrence of the phase transitions between the two polymorphs is presented in Hawthorne and Sokolova (2008).

Scapolites are common rock-forming or accessory minerals, mainly in metamorphic rocks of amphibolite or granulite facies (*e.g.* Stolz 1987; Oterdoom and Wenk 1983; Moecher and Essene 1991). Marialite-rich scapolites display an extended stability in lower metamorphic grade (*e.g.* Kwak 1977) or hydrothermally altered rocks, often in the presence of Cl-rich fluids which compositions are influenced by nearby evaporites (Satish-Kumar et al. 2006; Bernal et al. 2017; Pe-Piper et al. 2019; Morrisey and Tomkins 2020). The presence of SO_4-rich scapolites in granulite xenoliths of deep crustal origin hosted in magmatic rocks (Lovering and White 1964; Boivin and Camus 1981; Stolz 1987; Torrò et al. 2018) suggest they are stable and abundant at lower crust conditions (Lovering and White 1964; Hammerli et al. 2017; Porter and Austrheim 2017), as also suggested by the experimentally determined *P*-*T* stability fields of Goldsmith and Newton (1977). The break-down of SO_4-rich scapolites during retrograde metamorphism (*e.g.* Lovering and White 1964; Porter and Austrheim 2017) may release S to the fluids, with significant implications for the crystallization of sulphides or dissolution of calcophile elements in S-rich fluids (Porter and Austrheim 2017; Morrisey and Tomkins 2020).

In a previous study, Lotti et al. (2018) described the high-pressure behavior of an intermediate member of the marialite-meionite solid solution, characterized by an unconventional *I*-centered lattice at ambient conditions, possibly due to the presence of anti-phase domains (Seto et al. 2004) as discussed more in detail in section 4.1. In this work, we extend the study of that sample to non-ambient temperatures (at ambient-*P*), by means of *in situ* single-crystal (SC-XRD), powder X-ray diffraction (pw-XRD) and single-crystal neutron diffraction experiments. Moreover, a combined high-*T* and high-*P* *in situ* synchrotron SC-XRD investigation, using a resistive-heated diamond anvil cell, was performed. The major goals of this study are to: 1) investigate the effect of the crystal chemistry of scapolites on their thermal and compressional behavior, 2) describe the

structural deformation mechanisms at the atomic scale and 3) check the stability of the unconventional *I*4/*m* symmetry of the investigated sample at varying *T* and *P*.

1.1 Crystal structure of scapolite

The crystal structure of scapolite was first described by Pauling (1930) and Schiebold and Seumel (1932). Scapolites share structural features with zeolites and feldspathoids and can be defined as microporous compounds, as they show an open-framework of aluminosilicate tetrahedra characterized by channels and cages (Figures 1 and 2). The unidirectional channels (parallel to [001]) and the strong interactions among the extra-framework population, given by the combined presence of cations and anions, prevent scapolites to display the typical zeolitic physical-chemical properties (*e.g*. Gatta et al. 2018), showing, in this respect, a strong similarity with another group of microporous anions-bearing minerals with unidirectional channels, *i.e.* cancrinites (Lotti et al. 2012; Gatta and Lotti 2016). In both polymorphs of scapolite, the elliptical 8-membered ring channels are occupied by cations (Na and/or Ca with minor K) at the *M* site (Figure 1), whereas the anions (Cl, CO_3 or SO_4) occupy the cages centered on the tetragonal axis, each one neighboring with four symmetry-equivalent channels (Figures 1 and 2). In the *I*4/*m* polymorph, two independent *T* sites occur in the tetrahedral framework (Figure 1), with Al preferentially ordered at *T*2. In the intermediate members of the marialite-meionite solid solution series with $P4_2/n$ symmetry (*i.e.* between Me_{22} and Me_{78} according to the Me% formalism, Hawthorne and Sokolova 2008), *T*2 splits into *T*2 and *T*3, with a preferential ordering of Al at the former site due to a coupled interaction with a short-range ordering of the $Na_2Ca_2(Cl,CO_3)$ clusters (a detailed discussion is in Hawthorne and Sokolova 2008). Approaching the Al-rich compositions of meionite, the cations ordering effectiveness decreases and Al enters *T*3 as well, until the *I*4/*m* structure becomes the most stable polymorph again. In the present study, an intermediate member (*i.e.* Me_{48}) with an unexpected *I*4/*m* symmetry is investigated.

2. Materials and experimental methods

2.1. Sample and chemical analysis

A transparent single crystal of natural scapolite from Madagascar, *ca.* 1 cm in diameter, belonging to the mineralogical collection of Dr. Renato Pagano (Milan), was chosen for this experiment. Unfortunately, no more precise information on the occurrence of the sample are available. Several fragments were cut and checked under a polarized-light microscope, in order to exclude the presence of impurities, inclusions and optical defects. Four of the largest fragments were selected for the chemical analysis with an electron microprobe in wavelength dispersive mode (EPMA-WDS). The average chemical formula is: $(Na_{1.86}Ca_{1.86}K_{0.23}Fe_{0.01})(Al_{4.36}Si_{7.64})O_{24}[Cl_{0.48}(CO_3)_{0.48}(SO_4)_{0.01}]$. More details on the adopted experimental protocol are reported in Lotti et al. (2018).

2.2 In situ high-temperature synchrotron X-ray powder diffraction

Several fragments of the starting single crystal were finely ground in an agate mortar and the resulting powder loaded in a SiO_2-glass capillary (300 μm in diameter) for *in situ* high-*T* synchrotron X-ray powder diffraction experiments at the MCX beamline of ELETTRA synchrotron facility (Basovizza, Trieste, Italy). The beamline experimental setup is described in Rebuffi et al. (2014). During the data collections, the capillary was kept spinning, in order to maximize the random orientations of the crystallites. Twenty-one data collections were performed, at 25°C and from 50 to 1000°C in 50 °C increments, using a gas-blower to increase temperature. The monochromatic (λ = 0.827 Å) X-ray diffracted patterns were collected using the high-resolution scintillator detector available at the beamline, covering an angular range from 5° to 50°, with 0.008° step and 1 s exposure time per step.

Rietveld full-profile fits were performed using the EXPGUI (Toby 2001) interface of GSAS (Larson and Von Dreele 2004). The atomic positions reported by Lotti et al. (2018) for the same scapolite sample were used as starting structure model for the Rietveld refinement based on the 25 °C data, whereas, at any higher temperature, the starting model was that refined from the previous *T*-point. In the final cycles of refinement, the following parameters were always simultaneously optimized: scale

factor, background profile (Chebyshev polynomial with 15 parameters), zero-shift, peak profiles (modelled using the pseudo-Voigt function of Thompson et al. 1988), unit-cell parameters, site coordinates and isotropic displacement parameters. The following restrictions were adopted: the cation site was refined with a mixed scattering curve of Na, Ca and K (occupancies fixed on the basis of the chemical analysis), the *T* sites were modelled with the X-ray scattering curve of Si, the Cl and CO_3 sites were fixed at the occupancy derived from the chemical analysis and at the positions reported by Lotti et al. (2018), and a common isotropic displacement parameter was refined. Selected calculated *vs.* observed X-ray diffraction profiles are shown in Figures S1-S4 (Supplementary materials) and the refined unit-cell parameters are reported in Table 1.

2.3 *In situ* high-temperature single-crystal X-ray diffraction

A single-crystal fragment, free of defects at the optical scale, *ca.* 120 x 80 x 60 μm^3, was selected for the *in situ* high-*T* X-ray diffraction experiments at the Institute of Mineralogy and Petrography of the University of Innsbruck (Austria), using a Stoe IPDS II diffractometer equipped with graphite-monochromatized Mo-*K*α radiation (from a sealed X-ray tube, operated at 50 kV and 40 mA), an image plate detector 340 mm in diameter and a computer-controlled HEATSREAM device for increasing temperature (Krüger and Breil 2009). Seven data collections were performed at 25, 150, 300, 450, 600, 750 and 797 °C, adopting a step-wise 180° ω-scan with 1° and 60 s per step. The collected frames were converted in order to be processed by the software *CrysalisPro* (Rigaku Oxford Diffraction 2020), which was used for peaks indexing, refinement of unit-cell parameters and intensity data reduction (absorption correction performed using the *ABSPACK* routine implemented in *CrysalisPro*).

Structure refinements based on the experimental intensity data were performed using the JANA2006 suite (Petříček et al. 2014), starting from the model reported by Lotti et al. (2018). Atomic coordinates and anisotropic displacement parameters were refined adopting the following assumptions and restraints: the cation and the *T* sites were modelled as described in section 2.2; atomic coordinates of

the Cl and CO_3 sites were refined restraining the C-O bond lengths to 1.30 ± 0.02 Å and the O-C-O angles to 120 ± 2°, their occupancy was fixed to the values derived from the chemical analysis and restrained to share a common isotropic displacement parameter. All the refinements converged with no significant correlations among the refined parameters. Statistical parameters of the structure refinements are reported in Table S1 (supplementary materials); important structural parameters are in Tables 2 and S2 and the refined structure models deposited as CIF files.

2.4 *In situ* low-temperature single-crystal X-ray diffraction

A single-crystal fragment, free of defects at the optical scale, *ca.* 150 x 100 x 70 μm^3, was selected for the *in situ* low-*T* X-ray diffraction analysis at the Institute of Mineralogy and Petrography of the University of Innsbruck (Austria), using an Oxford Diffraction Gemini R Ultra four-circle diffractometer, operating at 50 kV and 40 mA and equipped with a graphite-monochromatized Mo-*K*α radiation, a Ruby-CCD detector and an Oxford CryoSystems 700 series cryostat for low-*T* investigations. Five data collections were performed at 25, -25, -50, -75 and -100 °C, adopting step-wise ω-scans with 1 °/step and 25 s exposure time per frame, in order to maximize the reciprocal space coverage. The experimental data were treated with *CrysalisPro* for indexing, unit-cell refinement and intensity data reduction.

Structure refinements were performed using the JANA2006 suite adopting the same strategies as described in section 2.3. Statistical parameters of the structure refinements are reported in Table S1; important structural parameters are listed in Tables 2 and S2 and the refined structure models deposited as CIF files.

2.5 Neutron diffraction experiments

A fragment of the original crystal of scapolite, *ca.* 3.1 x 3.0 x 2.8 cm^3 in size, was used for the neutron diffraction experiments at the four-circle diffractometer HEiDi at the research neutron source FRM II of the Heinz Maier-Leibnitz Zentrum (MLZ) in Garching near Munich, Germany. The source

provides a maximum (undisturbed) thermal neutron flux density of $8 \cdot 10^{14}$ $cm^{-2}s^{-1}$, at a nominal thermal power of 20 MW. The HEiDi diffractometer is equipped with a ^3He single counter detector [Eurisys 73NH17/5X end window counter, 50 mm entrance window, 5 bar ^3He pressure and 170 mm active length for high detection probability (>90% at 0.8 Å), separation of γ radiation by pulse height discrimination]. An integrated slit system defines the cross section of the entrance window of the detector. Further details on the instrument setup are reported in Meven and Sazonov (2015). Intensity data of scapolite were collected first at 25 and then at 685 °C. Data at high temperature were collected using a small water-cooled mirror furnace designed by the sample environment group of FRM II, and following the protocol used by Gatta et al. (2010). The temperature precision of this H*T*-device is about ±1°C. The temperature of the scapolite crystal was slowly increased (~200 °C/h) from 25 to 685 °C and annealed for 3 hours prior to data collection.

At 25°C, two sets of intensity data were collected: the first one with a wavelength of the incident beam of 1.170(1) Å up to $2\theta_{max}$ =130° ($\sin(\theta)/\lambda$ = 0.77 $Å^{-1}$) (Ge-311 monochromator, 0.5 mm Er foil filter to suppress λ/3 contamination) and the second one with a wavelength of the incident beam of 0.7925(5) Å up to $2\theta_{max}$ =85° ($\sin(\theta)/\lambda$ = 0.85 $Å^{-1}$) (Ge-422 monochromator, 0.5 mm Er foil filter to suppress λ/2 contamination). Peak intensities were collected using pure ω-scan or ω-2θ scan strategy; two standard reflections were measured every 450 min throughout the experiment, and the intensity variation was within ±1.5σ(*I*). At 685°C, one set of intensity data was collected, using a pure ω-scan strategy, with a wavelength of the incident beam of 0.8750(5) Å up to $2\theta_{max}$ = 90° ($\sin(\theta)/\lambda$ = 0.81 $Å^{-1}$) (Cu-220 monochromator, 0.5 mm Er foil filter to suppress λ/2 contamination). At both temperatures, the reflection conditions confirmed that the space group *I*4/*m* was preserved. Integrated intensities were corrected for the Lorentz effect; absorption correction was found to be negligible. Further details pertaining to the data collections are reported in Table S1.

Structure refinements were performed using the SHELXL software (Sheldrick 2014), implemented in the WinGX suite of programs (Farrugia 2012). The neutron intensity data collected were first

processed in order to calculate the normalized structure factors (*E*'s) and their statistical distributions (using the program *E-STATISTICS*, implemented in the WinGX package; Farrugia 2012). The structure was found to be centrosymmetric at both temperatures. The anisotropic structure refinement was then performed in the space group *I*4/*m*, starting from the structure model obtained from the X-ray refinement (section 2.3). The neutron scattering lengths of C, O, Na, Al, Si, Cl, K, and Ca were used according to Sears (1986). The effects of secondary isotropic extinction were modelled following the Larson's formalism (Larson 1967), as implemented in SHELXL-97. The refinements were conducted with the following protocol:

1) The *T1* and *T2* were modelled with a mixed neutron scattering length of Si and Al, whose fractions were refined.

2) The *M* site was modelled with a mixed (Na+K+Ca) scattering length, based on the fraction of each mass from the chemical analysis.

3) The anionic sites were modeled with the neutron scattering length of Cl, C and O, with the site occupancies fixed on the basis of the chemical analysis. The Cl site was modelled anisotropically, whereas C and O only isotropically.

When convergence was achieved, no significant residual peaks were found in the final difference-Fourier map of the nuclear densities (Table S1). The final agreement index R_1(obs) was 0.0325 for 69 refined parameters and 1072 unique reflections with $F_o^2/\sigma(F_o^2)>3$ at 25 °C, and 0.0567 for 65 refined parameters and 800 unique reflections at 685 °C (Table S1). Atomic coordinates and displacement parameters are listed in the CIF files; relevant bond lengths and angles are listed in Tables 2 and S2.

2.6. *In situ* combined high-pressure and high-temperature synchrotron single-crystal X-ray diffraction

Combined *in situ* high-pressure and high-temperature synchrotron single-crystal X-ray diffraction experiments have been performed at the P02.2 beamline of the DESY-PETRA-III synchrotron facility (Hamburg, Germany), using a 4-pin graphite resistive-heated diamond anvil cell (Hwang et al., in review; Liermann et al. 2015). Two single-crystal fragments were selected to perform two independent H*P*H*T* ramps. For all ramps, the sample was loaded in the *P*-chamber (200 μm in diameter) obtained by spark-erosion of a rhenium gasket previously pre-indented to *ca.* 50 μm, along with a couple of ruby spheres and gold powder as pressure calibrants. Silicone oil was added as *P*-transmitting fluid. The DAC was equipped with Boehler-Almax diamond anvils, with 300 μm culets and 64° opening angle. It was kept in a vacuum vessel during the XRD data acquisition. Temperature was monitored by two Pt:Pt-Rh type R thermocouples positioned at opposite sides of the *P*-chamber, whereas pressure was initially calibrated using the ruby fluorescence shift (Mao et al. 1986) and at H*P*H*T* by using the *P-T-V* equation of state of gold (Dorogokupets and Dewaele 2007), monitoring the shifts of the (111), (200) and (220) diffraction lines. Experimental pressures and temperatures of both ramps are reported in Table 3. A monochromatic X-ray beam (42.7 keV, λ = 0.2904 Å) was used, and the diffracted patterns collected on a Perkin-Elmer XRD 1621 flat panel detector. The following strategy was adopted for all data collections: a step-wise ω-scan from -25° to +25°, with 0.5° step-size and 1s exposure time per frame. Experimental data were collected using an in-house script and then converted to the "Esperanto" format in order to be processed by *CrysAlisPro* (Rigaku Oxford Diffraction 2020; Rothkirch et al. 2013) for the peak indexing, unit-cell parameters refinement and intensity data reduction (corrected for Lorentz-polarization effects). Absorption effects, due to the DAC components, were corrected using the semi-empirical *ABSPACK* routine, implemented in *CrysAlisPro*.

Structure refinements were performed using the JANA2006 suite, starting from the model reported by Lotti et al. (2018) and based on the experimental intensities collected during the H*P*H*T* ramp #2, which provided the highest data quality. The same assumptions and restrictions described in section

2.3 were applied. At 650 °C, between 10.3 and 10.7 GPa, a phase transition to a triclinic polymorph (see sections 3.3 and 4.3) was observed; the refinement of the triclinic structure, based on the model reported by Lotti et al. (2018), was not successful due to low reflections/variables ratio. Statistical parameters of the structure refinements are reported in Table S3, significant structural parameters in Tables 4 and S4 and the refined structure models deposited as CIF files.

3. Results

3.1 Thermal elastic behavior

The refined unit-cell parameters of the studied scapolite as a function of temperature are reported in Table 1 and plotted in Figure 3. All data show that the thermal expansion of scapolite is accommodated only on the (001) plane, leaving the unit-cell edge along the **c** axis almost unaffected by temperature. No discontinuities in the thermal evolution of the *a* and *V* parameters can be observed within the *T*-range investigated (*i.e.* from -100 to 1000 °C). The unit-cell parameters refined on the basis of the H*T* single-crystal XRD data describe a comparable thermal evolution, within the experimental uncertainty, to that shown by the H*T* powder XRD data. Therefore, only the volumes refined from the H*T*-powder data and the L*T*-single-crystal data, normalized to their respective ambient-*T* values, were taken into account to describe the thermo-elastic behavior (Figure 3). The $V/V_{25°C}$ *vs*. *T* data were fitted by a modified version of the equation of state, reported by Pawley et al. (1996), using the software EoSFit7GUI (Gonzalez-Platas et al. 2016):

- $V(T) = V_{T\mathrm{ref}}[1 + a_0(T-T_{\mathrm{ref}}) - 2(10a_0+a_1)(\sqrt{T}-\sqrt{T_{\mathrm{ref}}})]$, (1)

where T_{ref} is the reference *T* (here 25 °C), $V_{T\mathrm{ref}}$ the unit-cell volume at T_{ref}, a_0 and a_1 are two refinable parameters. The least-squares fit yields the following values (Table 5): $(V/V_0)T_{\mathrm{ref}} = 0.99986(6)$ (*i.e.* $V_0 = 1115.88(7)$ Å^3), $a_0 = 2.67(8)\cdot10^{-5}$ K^{-1} and $a_1 = -1.03(13)\cdot10^{-4}$ K$^{-1/2}$, from which the thermal

expansion coefficient at ambient conditions is calculated, $\alpha_{V25°C} = 1/V_0 \cdot (\partial V/\partial T)_{1bar,25°C} = 1.74(4) \cdot 10^{-5}$ K^{-1}.

If the previous equation of state (hereafter EoS) is fitted only using high-*T* synchrotron powder data, the following parameters are retrieved (Table 5): $V_0 = 1115.93(9)$ Å^3, $a_0 = 2.72(10) \cdot 10^{-5}$ K^{-1} and $a_1 = -0.98(16) \cdot 10^{-4}$ $K^{-1/2}$ (with $\alpha_{V25°C} = 1.71(4) \cdot 10^{-5}$ K^{-1}).

3.2. Thermal structural behavior

3.2.1 *In situ* H*T* and L*T* single-crystal XRD experiments. The single-crystal X-ray diffraction data obtained at both high-*T* (up to 797 °C) and low-*T* (down to -100 °C) were firstly inspected to check possible violations of the systematic absences expected for the *I*4/*m* space group. For all the H*T* datasets, no violations of the expected extinction rules were observed (Figure 4). For the five L*T* datasets, the inspection of the reconstructed reciprocal lattice planes did not show any clear violation of the extinction rules. However, Table S5 reveals that a very minor fraction of the reflections (~ 1%) apparently violates the systematic extinctions conditions, which are expected to be lost following the *I*4/*m*-to-*P*4$_2$/*n* phase transition, and that the number of violating reflections slightly increases from ambient-*T* down to -100 °C. A tentative refinement in the *P*4$_2$/*n* space group has been tried, but without any improvement in the figure of merit. In addition, performing the data reduction of the experimental data at -100 °C assuming a primitive lattice leads to the addition of 880 independent reflections, of which only 11 with $I_{hkl}(\mathrm{sig}(I_{hkl}) \geq 3$. Therefore, despite hints of an *I*-to-*P* phase transition can be suggested, the structure refinements were always performed in the *I*4/*m* space group.

An analysis of the H*T* single-crystal refined structures with a selection of the H*T* Rietveld-refined models, showed that, within the experimental uncertainties, the two datasets provide comparable results. The deformation trends that can be described up to 797 °C, on the basis of the single-crystal data, continue with no saturation effects up to 1000 °C, based on the powder data. Therefore, only the single-crystal refinements at low and high temperatures have been considered for the analysis of

the *T*-induced structure evolution. A selection of significant structural parameters is reported in Figure 5 and Tables 2 and S2. The four independent *T*-O-*T* inter-tetrahedral angles all increase with increasing temperature. The *T*1 and *T*2 coordination polyhedral volumes do not show significant variations with temperature, except for a slight apparent contraction of the *T*2 polyhedron at high-*T*. The main deformation mechanism of the framework in the scapolite structure is an anti-clockwise rotation of the 4-membered rings (4mRs) made of *T*1 and *T*2 tetrahedra (*e.g.* Sokolova and Hawthorne 2008), which can be described through the variation of the *O*1-*O*4-*O*3 inter-tetrahedral angle shown in Figure 5. Figure 5 and Table 2 show a positive linear correlation between this angle and the temperature. As a result, the channels ellipticity decreases with *T*, driven by a significant expansion of the shortest channel diameter. At high temperatures, all *M* cation bonds with the framework oxygens expand, with the largest variations shown by *M*-*O*3 and *M*-*O*4′ (Figure 5 and Table S2). At low-*T,* the former bonds are the only ones showing a contraction with decreasing *T*, whereas *M*-*O*2 and *M*-*O*4″ remain constant within the experimental uncertainties (Figure 5 and Table S2).

3.2.2. Neutron diffraction experiments.

Two single-crystal neutron diffraction experiments were performed at ambient and at 685 °C, respectively, and the collected data showed no violations of the systematic absences expected for the *I*4/*m* space group. Relevant structural parameters from the room- and high-*T* structure refinements are reported in Tables 2 and S2. The model refined at 25 °C confirms a disordered Si and Al distribution among the *T*1 and *T*2 sites, where *T*1 is enriched in Si and *T*2 almost equally occupied by the two chemical species. The refined framework composition [$Al_{4.3(2)}Si_{7.7(2)}O_{24}$] matches, within the experimental uncertainties, with the one obtained by chemical analysis [$Al_{4.36}Si_{7.64}O_{24}$]. In order to check any possible change of the Si and Al ordering among the tetrahedral sites at high-*T*, the structure refinement based on the data collected at 685 °C was performed refining the Si- and Al-occupancies of *T*1 and *T*2. Table S6 shows however, that any potential change remains within the estimated

standard deviation. Consistently, the average <*T*1-*O*> and <*T*2-*O*> bond distances (Table S2) suggest no change in the Si/Al ordering among the *T* sites as a function of temperature. A comparative analysis of the refined structure models based on neutron diffraction data with those based on X-ray diffraction data, allows to deduce the same *T*-induced main deformation mechanisms, described in the section 3.2.1.

3.3. Scapolite behavior at combined *in situ* high-*P* and high-*T*.

The X-ray diffraction data collected from the two ramps performed at combined high-*P* and high-*T* were firstly checked in order to determine the symmetry of the investigated scapolite. All the patterns collected at the pressures and temperatures of ramp #1 and those of ramp #2, up to 650 °C and 10.30 GPa, confirm the starting *I*4/*m* space group (Figure 6 and Table 3), whereas the data collected at 650 °C and 10.71 GPa, and at higher pressures, show the transition to a triclinic polymorph. The latter, for a direct comparison with the tetragonal unit cell, was described in the unconventional *I*-1 space group setting (Table 3), as already reported by Lotti et al. (2018) for the same phase transition observed between 9.23 and 9.87 GPa at ambient temperature. It is worth noting that the diffraction intensities of the triclinic polymorph were observed to significantly decrease with increasing pressure from 10.71 to about 16 GPa.

Relevant structural parameters from selected refinements based on the H*P*H*T* data of ramp#2 are reported in Tables 4 and S4 and discussed in section 4.3. A tentative structure refinement of the triclinic polymorph was tried, based on the intensity data collected at 650 °C and 10.71 GPa and on the model reported by Lotti et al. (2018). The refinement converged with a final R_{obs} = 17.49% (which can be regarded as satisfactory, considering the very complex experimental conditions and restrictions), but unfortunately, the very low ratio between observed reflections ($I_{obs} > 3\sigma(I_{obs})$: 236) and refined variables (106) prevents any robust discussion of the refined structure model.

4. Discussion

4.1 Crystal structure and symmetry of the investigated scapolite

The crystal fragments of scapolite studied here were taken from the same sample studied at high pressure by Lotti et al. (2018), showing an unusual *I*4/*m* symmetry, although one would expect a primitive lattice based on the chemical composition, intermediate between the end members marialite and meionite (*e.g*. Sokolova and Hawthorne 2008). The X-ray diffraction analyses reported here, performed with both conventional and synchrotron sources, as well as the neutron diffraction data, further confirm the absence of a relevant number of diffraction peaks that would violate the systematic extinctions expected for an *I*-centered lattice. Despite this number slightly increases at the lowest temperatures here investigated, the experimental data do not support unambiguously a structure model in the $P4_2/n$ space group.

As reported by Lotti et al. (2018), previous transmission electron microscopy and electron diffraction analyses show that several primitive scapolites are characterized by anti-phase domains (*e.g*., Phakey and Ghose 1972; Oterdoom and Wenk 1983; Hassan and Buseck 1988; Seto et al. 2004). Several hypotheses have been proposed based on structural evidence. Oterdoom and Wenk (1983), for example, suggested that at any anti-phase boundary, along the unit cell space diagonal, a reversal of the Si/Al ordering at the *T*2 and *T*3 sites (and of the associated ordering of $Na_2Ca_2(Cl,CO_3)$ clusters, Hawthorne and Sokolova 2008) occurs, so that the bulk crystal would show an average *I*4/*m* symmetry. Hawthorne and Sokolova (2008) reported that if the domains are sufficiently small, they may not be detected by X-ray diffraction experiments, which would provide the pattern of the average *I*4/*m* structure and, as previously suggested by Lotti et al. (2018), this may be the case for the sample investigated here. Seto et al. (2004) suggested that anti-phase domains in primitive scapolites may arise from an *I*-to-*P* phase transition induced by cooling, implying a crystallization at high temperature in the *I*4/*m* space group, which is preserved (metastable) at ambient conditions only in the case of a rapid cooling, hindering the transition to the $P4_2/n$ space group polymorph. This is a further hypothesis for the origin of the *I*-centered scapolite of this study.

A further cooling of these metastable scapolites at lower temperatures (*i.e.*, below ambient conditions values) may promote the phase transition to the expected $P4_2/n$ crystal structure. Based on the previously discussed experimental data obtained at $T < 25$ °C, an initial slow-kinetics *I*-to-*P* phase transition can be hypothesized to occur at $T \leq -100$ °C, but an unambiguous conclusion in this respect cannot be drawn. Recently, Torrò et al. (2018) reported a powder X-ray diffraction analysis from a scapolite xenolith of mantle origin, hosted in the alkaline basalts of the Olot suite in the La Garrotxa volcanic field (Catalunya, Spain), whose composition, despite more shifted towards the meionite end-member with respect to the sample investigated in this study, falls within the reported stability field of $P4_2/n$ scapolites. However, based on the systematic extinctions, the authors refined the sample in the $I4/m$ space group. The same symmetry was reported for a further scapolite sample of similar composition and geological setting from Chuquet Genestoux (France, Peterson et al. 1979). If the nature and the geological settings of the scapolites studied by Torrò et al. (2018) and Peterson et al. (1979) are taken into account (*i.e.* xenoliths of mantle origin picked up by alkaline basaltic magmas during their ascent), along with the evidence of flash melting at their rims (Torrò et al. 2018), a metastable preservation of the $I4/m$ structure induced by a rapid cooling can be suggested. Furthermore, the stability (ore metastability) of the *I*-centered polymorph may also be ascribed to the disorder of the sulfate anions (Peterson et al. 1979; Torrò et al. 2018), given the significant SO_2 content of these xenolithic samples. Unfortunately, the incomplete information about the origin of the scapolite sample from Madagascar used in this study precludes any discussion on the potential relationship between its unusual *I*-centered symmetry (for an intermediate member of the marialite-meionite joint) and its geological history. Nevertheless, while the available data prevent any conclusive discussion, the results of this study, along with those of Peterson et al. (1979) and Torrò et al. (2018), suggest that the potential preservation of metastable $I4/m$ intermediate scapolites in geological settings compatible to a rapid cooling history deserves further considerations to gain a comprehensive understanding.

4.2 Thermo-elastic behavior and *T*-induced structural re-arrangement

In order to compare the thermo-elastic behavior of the investigated Me_{47} scapolite with that of other members of the solid solution, which were experimentally studied by high-*T* X-ray diffraction (Levien and Papike 1976; Graziani and Lucchesi 1982; Baker 1994; Kabalov et al. 1999; Antao and Hassan 2008a,b), it is necessary to adopt a common model to describe the experimental *V*-*T* patterns. In section 3.1, the thermo-elastic behavior of the investigated scapolite is described by means of a thermal equation of state (1), which allows to fit the *V*-*T* data by the simultaneous refinement of three independent variables: V_0, a_0 and a_1. Since not all the experimental data reported in the literature allow the simultaneous refinement of three independent variables, all the datasets (including the H*T* synchrotron powder data object of this study) were fitted by the simplified equation proposed by Pawley et al. (1996) and reported in Holland and Powell (1998):

- $V(T) = V_{T\mathrm{ref}}[1 + a_0(T-T_{\mathrm{ref}}) - 20a_0(\sqrt{T}-\sqrt{T_{\mathrm{ref}}})$; (2)

The refined a_0 parameters and the calculated $\alpha_{V25°C}$ for the different members of the scapolite solid solution are reported in Table 5 and shown in Figure 3. They yield the decrease of the bulk thermal expansivity along the solid solution from marialite to meionite, but a univocal trend cannot be determined. On the contrary, at a first approximation, two different trends can be observed: the first defined by the a_0 refined parameters based on the data reported by Graziani and Lucchesi (1982), Levien and Papike (1976) and of this study, whereas the second based on the data reported by Baker (1994) and Antao and Hassan (2008a,b). Baker (1994) already noted a mismatch between the elastic behaviors described in her study and those reported by Graziani and Lucchesi (1982), especially for meionite-rich members. In order to validate the consistency of the refined parameters based on the powder data of this study, the EoS (2) was also applied to fit the *V*-*T* data obtained by *in situ* H*T*

single-crystal XRD: the refined a_0 parameters based on powder and single-crystal data differ within 2σ (Table 5), confirming no instrumental bias for the results of this study.

Discussing the distribution of values in the diagram of Figure 3 is not straightforward, as neither a clear correlation with the reported crystal-chemistry or the single-crystal *vs*. polycrystalline nature of the samples could be found, nor seems the uncommon *I*4/*m* symmetry shown by our scapolite to be relevant in this respect. The same existence of two different trends is also ambiguous, as it can be interpreted as an artifact. Based on the available data it is not possible to draw a conclusion on this point. Nevertheless, some observations can be made: if we compare the thermal expansion coefficient at ambient-*T* ($\alpha_{V25°C}$) calculated by the EoS (1) fit to the H*T* powder data from this study ($1.72(4)\cdot10^{-5}$ K^{-1}) with that calculated on the basis of the EoS (2) fit of the same dataset ($1.39(1)\cdot10^{-5}$ K^{-1}), a significant difference is observed. This result raises the question if the EoS (2) model is sufficiently robust to describe the thermo-elastic behavior of the scapolite investigated here, especially in the *T*-range close to ambient conditions, and, as a consequence, on the significance of the data reported in Figure 3. In conclusion, the previous discussion points out the importance of re-investigating the behavior of scapolite solid solution members at various temperatures by means of modern experimental techniques, which allow the fit of high-resolution *V*-*T* patterns.

From the structural point of view, the refined models in the *T*-range -100 °C to 797 °C show that the bulk thermal expansion is accommodated only in the plane perpendicular to the tetragonal axis, by the tilting of the framework tetrahedra around the shared oxygen hinges. Tilting of tetrahedra is the most common mechanism adopted by open-framework compounds to accommodate volume variations at non-ambient conditions (*e.g.* Gatta et al. 2018). In scapolites, in particular, this can be described by the cooperative rotation of the two independent 4-membered rings of tetrahedra around the shared *O*4 atom (Figures 1 and 5), which was already described to accommodate volume expansion or contraction in response to different compositions (Papike and Stephenson 1966), temperatures (e.g. Levien and Papike 1976; Graziani and Lucchesi 1982) and pressures (Comodi et

al. 1990; Lotti et al. 2018). At increasing temperature, this mechanism induces the opening of the 8-membered ring channels along the shorter axis (Figure 1, Table 2) and affects the *M* cations coordination polyhedra with an expansion of the *M*-(*O*,*Cl*) bonds (Figure 2, Table S2). If we consider only the average bond length between the *M* cation and the framework oxygens (<*M*-*Of*>), we can calculate a fictive volume $<M\text{-}Of>^3$, which permits, at a first approximation, the description of the thermal expansion of the cations coordination environment. Since data do not allow the simultaneous refinement of three variables (required for EoS (1)), the $<M\text{-}Of>^3$ *vs*. temperature data have been fitted by EoS (2). The refinement provides a refined $a_0 = 10.4(3)\cdot10^{-5}$ K^{-1} ($\alpha_{V25°C} = 4.37(11)\cdot10^{-5}$ K^{-1}), which confirms the significant role played by the cations coordination environment in accommodating the bulk volume expansion alongside the framework tetrahedral tilting.

Compared to the [100] or [010] directions, the unit-cell edge parallel to the **c** axis remains substantially unaffected by temperature. However, a slight, but unambiguous, decrease along [001] can be observed between room-*T* and 250 °C (Figure 3, Table 1). The same behavior is confirmed also if the unit-cell parameters based on single-crystal XRD are considered. An inspection of the *T*-induced evolution of the inter-tetrahedral *T*-*O*-*T* angles (Figure 5, Table 2) shows that if *T*2-*O*3-*T*2 and *T*1-*O*4-*T*2 expands all over the investigated *T*-range, *T*2-*O*2-*T*2, which also experiences the largest expansion at 797 °C, stays constant at 25 and 150 °C. This behavior appears to affect mainly the diameters of the 4-membered rings made by the *T*1 tetrahedra (Table S2) and the *M*-*O*4″ and *M*-*Cl* bond lengths, which all show variations only at $T > 150$ °C. These findings suggest the onset of new tilting deformation mechanisms at $T \geq 250$ °C. A similar anomalous behavior along [001] was already observed for an almost pure marialite by Kabalov et al. (1999), and for a Me_{33} scapolite by Antao and Hassan (2008b), who assigned it to a disordering process of the Na and Ca atoms at the *M* site.

4.3 Behavior at combined high pressure and high temperature

Based on the experimental *V*-*P* data reported by Lotti et al. (2018), the *V*-*T* data of this study discussed in sections 3.2 and 4.2 and the *V*-*P*-*T* data described in section 3.3 (normalizing unit-cell volumes to the respective values at ambient conditions), it is possible to refine a *PVT*-equation of state that assumes an isothermal II-order Birch-Murnaghan EoS ($K_V' = 4$) formalism, the modified Holland-Powell thermal EoS reported in section 4.2 (Eq. 2) and a linear dK/dT, yielding the following parameters: $K_{V0} = 68.4(20)$ GPa, $a_0 = 3.33(2)\cdot 10^{-5}$ K^{-1} and $dK/dT = -0.016(7)$ GPa/K.

The deformation mechanisms acting at combined high-*P* and high-*T* are the same already described at high and low temperature (and ambient-*P*) in the previous section and at high pressure (and room-*T*) by Lotti et al. (2018). In particular, when *T* is < 500 °C, the effect of pressure appears to be dominant, with the anti-cooperative rotation of the 4mRs on the (001) plane, inducing a compression of the channels along the shorter axis with related increase in ellipticity (Table 4). At *T* > 500 °C, the deformation mechanisms induced by pressure are still dominant, but are partially counterbalanced by the opposite mechanisms induced by the increase in temperature, as can be deduced by the comparison of relevant structural parameters with those reported by Lotti et al. (2018) at $HP_{25°C}$ (Tables 4 and S4). As already observed in the isothermal compression of the same sample at 25 °C (Lotti et al. 2018), approaching the phase transition a saturation of the *M*-*O*4′ and *M*-*Cl* bond lengths takes place (Table S4).

The phase transition from the starting tetragonal *I*4/*m* to the triclinic *I*-1 polymorph has been detected at 650 °C at a pressure that is about 1 GPa higher than that at which it was observed at ambient temperature. This leads to a positive Clapeyron slope (*i.e.*, $dP/dT > 0$, Figure 6).

The triclinic polymorph is, nevertheless, stable (or metastable) at very high pressures for natural scapolites (~ 10 GPa). This consideration, along with the rapid decrease in intensity of the diffraction peaks in the *P*-*T* stability field of *I*-1 scapolite, suggests that the occurrence of the phase transition: 1) demonstrates the significant flexibility of the scapolite structure, which, as other open-framework compounds (*e.g.* Lotti et al. 2015a,b), adopts a displacive phase transition to accommodate the volume

compression when tetrahedra tilting is no longer sufficient, but 2) raises the question of whether the triclinic polymorph may actually occur in nature.

5. Implications

The results of this study, along with those reported by Lotti et al. (2018), provide accurate thermo-elastic parameters of an intermediate member of the marialite-meionite solid solution (Me_{47}): $\alpha_{V25°C}$ = 1.72(4)·10^{-5} K^{-1} and $\beta_{V0.0001GPa}$ = 0.0143(4) GPa^{-1}, as well as their evolution as a function of temperature and pressure, respectively, and a linear dK/dT = -0.016(7) GPa/K.

In addition, this study aimed at describing the variation of the thermo-elastic parameters as a function of the scapolite crystal chemistry by a comparison with literature data. This comparison further confirmed that, moving from marialite to meionite, a decrease in both the volume compressibility and bulk thermal expansivity occurs, the latter being extremely anisotropic. However, if a model, valid at a first approximation, of the β_V *vs.* Me% was possible (Lotti et al. 2018), the discussion of data reported in Figure 3 and Table 5 (see section 4.2) prevents the application of the same protocol to the thermal expansion coefficient. Eq(1) and Eq(2) applied to the same data yielded a different model of the *V*-*T* behavior at temperatures close to ambient values (cfr. calculated $\alpha_{V25°C}$ in Table 5). The data in Figure 3, calculated by adopting Eq(2), do not allow even a coarse modelling of the evolution of α_V as function of Me%. This evidence wards a re-investigation of the minerals behavior at non-ambient conditions, if more modern experimental techniques or instruments are available in order to use the most accurate EoS available. For a complex and non-binary solid solution like scapolite, for example, in order to model the influence of the crystal chemistry on the thermo-elastic parameters, a systematic re-investigation of the thermal behavior of the different solid solution members appears mandatory.

The structure refinements at variable conditions of temperature and pressure show that the structural stability of scapolite at the (*P*,*T*)-conditions of the lower crust and upper mantle is facilitated by a

non-destructive deformation mechanisms at the atomic scale (basically tetrahedral tilting) able to efficiently accommodate the bulk volume variations, as the only observed phase transition in the investigated (P,T)-ranges occur at very high pressures, outside the phase stability field of scapolite in nature.

The uncommon $I4/m$ symmetry of the investigated sample of intermediate scapolite apparently does not have a significant impact on its behavior at non-ambient conditions. The X-ray and neutron diffraction data presented in this study show that the investigated sample preserves the I-centered lattice at high T, whereas an apparent transition to a primitive lattice may occur when approaching the lowest investigated temperature of -100 °C. These results, along with those of Peterson et al. (1979) and Torrò et al. (2018) (see section 4.1), suggest that the possible crystallization of intermediate scapolites in the $I4/m$ space group at high temperatures (and pressures) should be further investigated, as well as the potential phase transition temperature and influence of the cooling rate on the metastable preservation of I-centered scapolites. In fact, the persistence at ambient conditions of metastable $I4/m$ intermediate scapolites (or $P4_2/n$ scapolites with average $I4/m$ diffraction pattern due to small anti-phase domains) may provide indirect information on the thermal history of the hosting rocks and of the rocks in which they formed.

6. Acknowledgments

An anonymous reviewer is thanked for the competent and useful comments that improved the manuscript. We are grateful to Dr. Renato Pagano for providing the scapolite sample from his private mineralogical collection. We acknowledge DESY (Hamburg, Germany), a member of the Helmholtz Association HGF, for the provision of experimental facilities. Parts of this research were carried out at PETRA-III and beamtime was allocated for proposal I-20170565 EC. The research leading to this result has been supported by the project CALIPSOplus under the Grant Agreement

730872 from the EU Framework Programme for Research and Innovation HORIZON 2020. ELETTRA Sincrotrone Trieste is acknowledged for the provision of beamtime and synchrotron facilities at the MCX beamline. Part of this work is based upon experiments performed at the HEiDi instrument operated jointly by RWTH Aachen University and Forschungszentrum Jülich within the JARA-FIT collaboration at the Heinz Maier-Leibnitz Zentrum (MLZ), Garching, Germany.

The authors acknowledge the support by the Italian Ministry of Education (MIUR) through the project ‘‘PRIN2017 - Mineral reactivity, a key to understand large-scale processes” (2017L83S77). PL and GDG acknowledge the University of Milan for financial support through the project “Piano di Sostegno alla Ricerca 2021”.

7. References

Antao, S.M., and Hassan, I. (2008a) Unusual Al-Si ordering in calcic scapolite, $Me_{79.6}$, with increasing temperature. American Mineralogist, 93, 1470-1477.

Antao, S.M., and Hassan, I. (2008b) Increase in Al-Si and Na-Ca disorder with temperature in scapolite $Me_{32.9}$. Canadian Mineralogist, 46, 1577-1591.

Baker, J. (1994) Thermal expansion of scapolite. American Mineralogist, 79, 878-884.

Bernal, N., Gleeson, S.A., Smith, M.P., Barnes, J.D., and Pan, Y. (2017) Evidence of multiple halogen sources in scapolites from iron oxide-copper-gold (IOCG) deposits and regional Na-Cl metasomatic alteration, Norrbotten County, Sweden. Chemical Geology, 451, 90–103.

Boivin, P., and Camus, G. (1981) Igneous scapolite-bearing associations in the Chaîne des Puys, Massif Central (France) and Atakor (Hoggar, Algeria). Contributions to Mineralogy and Petrology, 77, 365-375.

Comodi, P., Mellini, M., and Zanazzi. P.F. (1990) Scapolites: variation of structure with pressure and possible role in the storage of fluids. European Journal of Mineralogy, 2, 195–202.

Dorogokupets, P.I., and Dewaele, A. (2007) Equations of state of MgO, Au, Pt, NaCl-B1, and NaCl-B2: Internally consistent high-temperature pressure scales. High Pressure Research 27, 431-446.

Evans, B.W., Shaw, D.M., and Haughton, D.R. (1969). Contributions to Mineralogy and Petrology, 24, 293-305.

Farrugia, L.J. (2012) WinGX and ORTEP for Windows: an update. Journal of Applied Crystallography, 45, 849-854.

Gatta G.D., and Lotti, P. (2016) Cancrinite-group minerals: crystal-chemical description and properties under non-ambient conditions - a review. American Mineralogist, 101, 253–265.

Gatta, G.D., Meven, M., and Bromiley, G. (2010) Effects of temperature on the crystal structure of epidote: a neutron single-crystal diffraction study at 293 and 1,070 K. Physics and Chemistry of Minerals, 37, 475-485.

Gatta, G.D., Lotti, P., and Tabacchi, G. (2018) The effect of pressure on open framework silicates: elastic behaviour and crystal–fluid interactions. Physics and Chemistry of Minerals, 45, 115–138.

Goldsmith, J.R., and Newton, R.C. (1977) Scapolite-plagioclase stability relations at high pressures and temperatures in the system $NaAlSi_3O_8$-$CaAl_2Si_2O_8$-$CaCO_3$-$CaSO_4$. American Mineralogist, 62, 1063-1081.

Gonzalez-Platas, J., Alvaro, M., Nestola, F., and Angel, R.J. (2016) EosFit7-GUI: a new graphical user interface for equation of state calculations, analyses and teaching. Journal of Applied Crystallography, 49, 1377–1382.

Graziani, G., and Lucchesi, S. (1982) The thermal behavior of scapolites. American Mineralogist, 67, 1229-1241.

Hammerli, J., Kemp, A.I.S., Barrett, N., Wing, B.A., Roberts, M., Arculus, R.J., Boivin, P., Nude, P.M., and Rankenburg, K. (2017) Sulfur isotope signatures in the lower crust: a SIMS study on S-rich scapolites on granulites. Chemical Geology, 454, 54–66.

Hassan, I., and Buseck, P.R. (1988) HRTEM characterization of scapolite solid solutions. American Mineralogist, 73, 119–134.

Hawthorne F.C., and Sokolova, E.V. (2008) The crystal chemistry of the scapolite-group minerals. II. The origin of the $I4/m \leftrightarrow P4_2/n$ phase transition and the nonlinear variations in chemical composition. Canadian Mineralogist 46, 1555–1575

Holland, T.J.B., and Powell, R. (1998) An internally consistent thermodynamic data set for phases of petrological interest. Journal of Metamorphic Geology, 16, 309-343.

Hwang, H., Bang, Y., Choi, J., Cynn, H., Jenei, Z., Evans, W.J., Ehnes, A., Schwark, I., Glazyrin, K., Gatta, G.D., Lotti, P., Sanloup, C., Lee, Y., and Liermann, H-P., Graphite Resistive heated ìDiamond Anvil Cell for simultaneous high-pressure and -temperature diffraction experiments. Review of Scientific Instruments, in review.

Kabalov, Y.K., Sokolova, E.V., Kalygina, N.V., and Schneider, J. (1999) Changes in the Crystal Structure of Marialite during Heating. Structure of Inorganic Compounds, 44, 979-983.

Krüger, H, and Breil, L. (2009) Computer-controlled high-temperature single-crystal X-ray diffraction experiments and temperature calibration. Journal of Applied Crystallography, 42, 140-142.

Kwak, T.A.P. (1977) Scapolite compositional change in a metamorphic gradient and its bearing on the identification of meta-evaporite sequences. Geological Magazine, 114, 343-354.

Larson, A.C. (1967) Inclusion of secondary extinction in least-squares calculations. Acta Crystallographica, 23, 664-665.

Larson, A.C., and Von Dreele, R.B. (2004) GSAS, General Structure Analysis System. Report LAUR 86-748. Los Alamos National Laboratory.

Levien, L., and Papike, J.J. (1976) Scapolite crystal chemistry: aluminum-silicon distributions, carbonate group disorder, and thermal expansion. American Mineralogist, 61, 864-877.

Liermann, H-P., Konôpková, Z., Morgenroth, W., Glazyrin, K., Bednarcik, J., McBride, E.E., Petitgirard, S., Delitz, J.T., Wendt, M., Bican, Y., Ehnes, A., Schwark, I., Rothkirch, A., Tischer, M., Heuer, J., Schulte-Schrepping, H., Kracht, T, and Franz, H. (2015) The Extreme Conditions Beamline P02.2 and the Extreme Conditions Science Infrastructure at PETRA III. Journal of Synchrotron Radiation 22, 908-924.

Lotti, P., Gatta, G.D., Rotiroti, N., and Cámara, F. (2012) High-pressure study of a natural cancrinite. American Mineralogist, 97, 872-882.

Lotti, P., Gatta, G.D., Merlini, M., and Liermann, H-P. (2015a) High-pressure behavior of synthetic mordenite-Na: an in situ single-crystal synchrotron X-ray diffraction study. Zeitschrift fűr Kristallographie, 230, 201–211.

Lotti, P., Arletti, R., Gatta, G.D., Quartieri, S., Vezzalini, G., Merlini, M., Dmitriev, V., and Hanfland, M. (2015b) Compressibility and crystal-fluid interactions in all-silica ferrierite at high pressure. Microporous and Mesoporous Materials, 218, 42–54.

Lotti, P., Comboni, D., Merlini, M., and Hanfland, M. (2018) High-pressure behavior of intermediate scapolite: compressibility, structure deformation and phase transition. Physics and Chemistry of Minerals, 45, 945-962.

Lovering, J.L., and White, J.R. (1964) The Significance of Primary Scapolite in Granulitic Inclusions from Deep-seated Pipes. Journal of Petrology, 5, 195-218.

Mao, H.K., Xu, J., and Bell, P.M. (1986) Calibration of the ruby gauge to 800 kbar under quasihydrostatic conditions. Journal of Geophysical Research, 91, 4673–4676.

Meven, M., and Sazonov, A. (2015) HEiDi: Single crystal diffractometer at hot source. Journal of large-scale research facilities, 1, A7.

Moecher, D.P., and Essene, E.J. (1991) Calculation of CO_2 activities using scapolite equilibria: constraints on the presence and composition of a fluid phase during high grade metamorphism. Contributions to Mineralogy and Petrology, 108, 219-240.

Momma, K., and Izumi, F. (2011) Vesta 3 for three-dimensional visualization of crystal, volumetric and morphology data. Journal of Applied Crystallography, 44, 1272–1276.

Morrisey, L.J., and Tomkins, A.G. (2020) Evaporite-bearing orogenic belts produce ligand-rich and diverse metamorphic fluids. Geochimica and Cosmochimica Acta, 275, 163-187.

Oterdoom, W.H., and Wenk, H-R. (1983) Ordering and composition of scapolite: field observations and structural interpretations. Contributions to Mineralogy and Petrology, 83, 330–341.

Papike, J.J., and Stephenson, N.C. (1966) The crystal structure of mizzonite, a calcium- and carbonate-rich scapolite. American Mineralogist, 51, 1014–1027.

Pauling, L. (1930) The structure of some sodium and calcium aluminosilicates. Proceedings of the National Academy of Sciences, 16, 453–459.

Pawley, A.R., Redfern, S.A.T., and Holland, T.J.B. (1996) Volume behavior of hydrous minerals at high pressure and temperature: I. Thermal expansion of lawsonite, zoisite, clinozoisite, and diaspore. American Mineralogist, 81, 335-340.

Pe-Piper, G., Piper, D.J.W., and Nagle, J. (2019) Scapolite and analcime: Monitors of magmatic fluid metasomatism in a major shear zone. Chemical Geology, 522, 208-222.

Peterson, R.C., Donnay, G., and Le Page, Y. (1979) Sulfate disorder in scapolite. Canadian Mineralogist, 17, 53-61.

Petříček, V., Dušak, M., and Palatinus, L. (2014) Crystallographic computing system JANA2006: general features. Zeitschrift fűr Kristallographie, 229, 345–352.

Phakey, P.P., and Ghose, S. (1972) Scapolite: observation of anti-phase domain structure. Nature Physics, 238, 78–80.

Porter, J.K., and Austrheim, H. (2017) Sulphide formation from granulite facies S-rich scapolite breakdown. Terra Nova, 29, 29–35.

Rebuffi, L., Plaisier, J.R., Abdellatief, M., Lausi, A., and Scardi, P. (2014) MCX: a Synchrotron Radiation Beamline for X-ray Diffraction Line Profile Analysis. Zeitschrift für anorganische und allgemeine Chemie, 640, 3100-3106.

Rigaku Oxford Diffraction, (2020), CrysAlisPro Software system, version 1.171.40_64.67, Rigaku Corporation, Wroclaw, Poland.

Rothkirch, A., Gatta, G.D., Meyer, M., Merkel, S., Merlini, M., and Liermann, H-P. (2013) Single-crystal diffraction at the Extreme Conditions beamline P02.2: procedure for collecting and analyzing high-pressure single-crystal data. Journal of Synchrotron Radiation, 20, 711-720.

Satish-Kumar, M., Hermann, J., Tsunogae, T., and Osanai, Y. (2006) Carbonation of Cl-rich scapolite boudins in Skallen, East Antarctica: evidence for changing fluid condition in the continental crust. Journal of Metamorphic Geology, 24, 241–261.

Schiebold, E., and Seumel, G. (1932)Űber die Kristallstruktur von Skapolith. Zeitschrift fűr Kristallographie, 81, 110–134 (in German).

Sears, V.F. (1986) Neutron scattering lengths and cross-sections. In K. Sköld and D.L. Price, Eds., Neutron Scattering, Methods of Experimental Physics, p. 521-550. Vol. 23A, Academic Press, New York.

Seto, Y., Shimobayashi, N., Miyake, A., and Kitamura, M. (2004) Composition and $I4/m$ -$P4_2/n$ phase transition in scapolite solid solutions. American Mineralogist, 89, 257-265.

Shaw, D.M. (1960a) The Geochemistry of Scapolite Part I. Previous Work and General Mineralogy. Journal of Petrology, 1, 218-260.

Shaw D.M. (1960b) The Geochemistry of Scapolite: Part II. Trace Elements, Petrology, and General Geochemistry. Journal of Petrology, 1, 261-285.

Sheldrick, G.M. (2014) SHELXT: Integrating space group determination and structure solution. Acta Crystallographica, A70, C1437.

Sokolova, E.V., and Hawthorne, F.C. (2008) The crystal chemistry of the scapolite-group minerals. I. Crystal structure and long-range order. Canadian Mineralogist, 46, 1527–1554.

Stolz, A.J. (1987) Fluid activity in the lower crust and upper mantle: mineralogical evidence bearing on the origin of amphibole and scapolite in ultramafic and mafic granulite xenoliths. Mineralogical Magazine, 51, 719-732.

Teerstra, D.K., and Sheriff, B.L. (1997) Substitutional mechanisms, compositional trends and the end-member formulae of scapolite. Chemical Geology, 136, 233–260.

Thompson, P., Cox, D.E., and Hastings, J.B. (1988) Rietveld refinement of Debye-Scherrer synchrotron X-ray data from Al_2O_3. Journal of Applied Crystallography, 20, 79-83.

Toby, B.H. (2001) EXPGUI, a graphical user interface for GSAS. Journal of Applied Crystallography, 34, 210-213.

Torró, L., Martin, R.F., Schumann, D., Cox, J., Galì Medina, S., and Melgarejo Draper, J.C. (2018) The incipient flash melting of scapolite and plagioclase megacrysts in alkali basalts of the Olot suite, Catalunya, Spain, and at Chuquet Genestoux, Puy-de-Dôme, France. European Journal of Mineralogy, 30, 45-59.

Zolotarev, A.A. (1996) Once more about the schemes and rows of isomorphism within the scapolite group. Zapiski Vserossiiskogo Mineralogicheskogo Obshchestva,125, 69–73 (in Russian).

Table 1. Unit-cell parameters of scapolite at different temperatures.

Experiment	*T* (°C)	*a* (Å)	*c* (Å)	*V* (Å^3)	*c*/*a*
Powder H*T*	25	12.13784(6)	7.57525(5)	1116.040(15)	0.624102(7)
Powder H*T*	50	12.14000(6)	7.57473(5)	1116.365(15)	0.623948(7)
Powder H*T*	100	12.14605(6)	7.57446(5)	1117.433(15)	0.623615(7)
Powder H*T*	150	12.15209(6)	7.57415(4)	1118.500(14)	0.623280(6)
Powder H*T*	200	12.15761(6)	7.57357(5)	1119.430(15)	0.622949(7)
Powder H*T*	250	12.16441(6)	7.57365(4)	1120.696(15)	0.622607(6)
Powder H*T*	300	12.16937(6)	7.57265(4)	1121.460(14)	0.622271(6)
Powder H*T*	350	12.17569(6)	7.57259(4)	1122.617(15)	0.621943(6)
Powder H*T*	400	12.18267(6)	7.57298(4)	1123.964(14)	0.621619(6)
Powder H*T*	450	12.18792(6)	7.57254(4)	1124.866(14)	0.621315(6)
Powder H*T*	500	12.19538(5)	7.57312(4)	1126.330(14)	0.620983(6)
Powder H*T*	550	12.20193(5)	7.57308(4)	1127.534(14)	0.620646(6)
Powder H*T*	600	12.20785(5)	7.57300(4)	1128.615(14)	0.620339(6)
Powder H*T*	650	12.21409(6)	7.57281(4)	1129.743(14)	0.620006(6)
Powder H*T*	700	12.22150(6)	7.57320(4)	1131.172(14)	0.619662(6)
Powder H*T*	750	12.22818(6)	7.57343(4)	1132.433(15)	0.619342(6)
Powder H*T*	800	12.23419(6)	7.57338(4)	1133.547(15)	0.619034(6)
Powder H*T*	850	12.24068(6)	7.57348(5)	1134.766(15)	0.618714(7)
Powder H*T*	900	12.24646(6)	7.57318(5)	1135.793(15)	0.618397(7)
Powder H*T*	950	12.25291(6)	7.57351(5)	1137.041(15)	0.618099(7)
Powder H*T*	999	12.25855(6)	7.57381(5)	1138.13(2)	0.617839(7)
SC-H*T*	25	12.1306(2)	7.5690(2)	1113.79(3)	0.62396(2)
SC-H*T*	150	12.1421(2)	7.5677(2)	1115.71(3)	0.62326(2)
SC-H*T*	300	12.1592(2)	7.5667(2)	1118.71(3)	0.62230(2)
SC-H*T*	450	12.1779(2)	7.5669(2)	1122.18(3)	0.62136(2)
SC-H*T*	600	12.1964(2)	7.5659(2)	1125.43(3)	0.62034(2)
SC-H*T*	750	12.2212(2)	7.5690(2)	1130.49(3)	0.61933(2)
SC-H*T*	797	12.2252(2)	7.5678(2)	1131.04(4)	0.61903(3)

SC-L*T*	25	12.1430(4)	7.5814(5)	1117.89(10)	0.62434(6)
SC-L*T*	-25	12.1352(4)	7.5800(5)	1116.25(9)	0.62463(6)
SC-L*T*	-50	12.1334(4)	7.5810(5)	1116.09(9)	0.62480(6)
SC-L*T*	-75	12.1300(4)	7.5825(5)	1115.67(9)	0.62510(6)
SC-L*T*	-100	12.1284(4)	7.5817(4)	1115.25(8)	0.62512(5)
ND	25	12.1378(1)	7.5753(1)	1116.04(2)	0.62411(1)
ND	685	12.2191(2)	7.5729(2)	1130.68(5)	0.61976(3)

Powder H*T:* data based on *in-situ* high-temperature powder X-ray diffraction experiments; SC-H*T*: data based on *in-situ* high-temperature single-crystal X-ray diffraction experiments; SC-L*T:* data based on *in-situ* low-temperature single-crystal X-ray diffraction experiments; ND: data based on *in-situ* high-temperature single-crystal neutron diffraction experiments.

Table 2. Selected angles (°), distances (Å) and polyhedral volumes (Å^3) from the refined structure models of scapolite at different temperatures (see text for further details).

Experiment	*T* (°C)	*T*1-*O*1-*T*1	*T*2-*O*2-*T*2	*T*2-*O*3-*T*2	*T*1-*O*4-*T*2	*O*1-*O*4-*O*3	8mR *O*4-*O*4	8mR *O*4-*O*4	8mR ε*	*V*(*M*)**
SC-HT	25	158.5(2)	139.66(4)	146.9(2)	137.3(2)	93.59(6)	3.148(5)	9.329(5)	0.3374(7)	19.12(6)
SC-HT	150	158.4(2)	139.67(4)	146.9(2)	137.3(2)	93.81(6)	3.162(5)	9.320(5)	0.3393(7)	19.23(6)
SC-HT	300	158.5(2)	139.85(4)	147.1(2)	137.4(2)	94.16(7)	3.184(5)	9.311(5)	0.3420(7)	19.38(6)
SC-HT	450	158.6(2)	140.09(4)	147.2(2)	137.6(2)	94.51(6)	3.211(5)	9.301(5)	0.3452(7)	19.57(7)
SC-HT	600	158.7(2)	140.29(4)	147.3(2)	137.8(2)	94.89(6)	3.240(5)	9.290(5)	0.3488(7)	19.77(7)
SC-HT	750	158.8(3)	140.48(4)	147.5(2)	137.9(2)	95.22(7)	3.265(5)	9.289(5)	0.3515(7)	19.97(7)
SC-HT	797	158.8(2)	140.50(4)	147.6(2)	138.0(2)	95.37(7)	3.274(5)	9.283(5)	0.3527(7)	20.03(7)
SC-LT	25	158.3(2)	139.82(3)	146.76(13)	137.24(11)	93.58(5)	3.146(4)	9.340(4)	0.3368(6)	19.16(4)
SC-LT	-50	158.2(2)	139.78(3)	146.72(12)	137.24(10)	93.45(5)	3.134(4)	9.343(4)	0.3354(6)	19.08(4)
SC-LT	-100	158.2(2)	139.68(3)	146.67(11)	137.26(11)	93.37(5)	3.128(4)	9.345(4)	0.3347(6)	19.03(4)
ND	25	158.26(3)	139.67(2)	147.00(2)	137.41(2)	93.69(1)	3.148(1)	9.330(1)	0.3374(1)	19.16(2)
ND	685	158.04(12)	140.17(6)	147.69(9)	137.60(9)	95.35(3)	3.263(3)	9.286(3)	0.3514(4)	19.97(7)

* defined as (8mR *O*4-*O*4 short)/(8mR *O*4-*O*4 long); ** volume of the *M* cation coordination polyhedron calculated using the tools implemented in VESTA3 (Momma and Izumi 2011)

Table 3a. Unit-cell parameters of tetragonal scapolite at different combined high-pressures and temperatures conditions.

Ramp	*T* (°C)	*P* (GPa)	*a* (Å)	*c* (Å)	*V* (Å^3)	*c*/*a*
1	25	3.43	11.897(3)	7.480(6)	1058.7(9)	0.6287(7)
1	200	5.22	11.823(2)	7.472(3)	1044.5(5)	0.6320(3)
1	400	5.78	11.839(2)	7.456(3)	1045.1(5)	0.6298(4)
1	400	6.62	11.742(3)	7.441(4)	1026.0(7)	0.6337(5)
1	400	7.70	11.667(3)	7.477(6)	1017.7(9)	0.6409(7)
1	400	7.85	11.640(3)	7.457(6)	1010.4(9)	0.6406(7)
1	400	8.00	11.651(5)	7.483(6)	1016(1)	0.6423(8)
1	400	8.68	11.561(5)	7.447(7)	995(1)	0.6441(9)
1	400	9.11	11.530(5)	7.448(9)	990(1)	0.6460(11)
2	25	0.0001	12.1136(3)	7.5588(3)	1109.2(1)	0.62399(4)
2	25	1.27	12.0273(5)	7.5228(4)	1088.2(1)	0.62548(6)
2	25	1.42	12.0235(4)	7.514(2)	1086.3(2)	0.6250(2)
2	100	1.92	11.9869(8)	7.5117(7)	1079.3(1)	0.62666(10)
2	200	3.64	11.9497(13)	7.4733(14)	1067.1(3)	0.6254(2)
2	300	4.67	11.8578(5)	7.4491(4)	1047.4(1)	0.62820(6)
2	400	5.68	11.8541(5)	7.4422(4)	1045.8(1)	0.62782(6)
2	500	6.35	11.8371(4)	7.4273(4)	1040.7(1)	0.62746(5)
2	650	8.98	11.7378(5)	7.364(2)	1014.6(3)	0.6274(2)
2	650	9.41	11.7280(5)	7.311(2)	1005.6(3)	0.6234(2)
2	650	10.30	11.7206(11)	7.289(5)	1001.3(6)	0.6219(5)

Table 3b. Unit-cell parameters of triclinic scapolite at different combined high-pressures and temperatures conditions.

Ramp	*T* (°C)	*P* (GPa)	*a* (Å)	*b* (Å)	*c* (Å)	*α* (°)	*β* (°)	*γ* (°)	*V* (Å^3)	*c/a*
2	650	10.71	11.714(4)	11.556(5)	7.319(3)	88.05(12)	89.88(6)	89.67(5)	990(2)	0.6248(5)
2	650	11.78	11.673(5)	11.573(11)	7.132(6)	86.86(7)	90.57(6)	89.72(6)	962(1)	0.6110(8)
2	650	12.93	11.684(5)	11.503(14)	7.164(7)	86.51(9)	90.26(6)	89.62(6)	961(1)	0.6131(9)
2	650	13.11	11.638(7)	11.507(11)	7.077(6)	86.19(7)	90.89(8)	89.51(7)	946(1)	0.6081(9)
2	650	14.36	11.619(9)	11.485(13)	7.103(8)	86.22(9)	90.94(10)	89.44(9)	946(2)	0.6113(12)
2	650	14.63	11.616(11)	11.40(2)	6.690(10)	85.05(12)	91.38(11)	88.97(10)	917(2)	0.5759(14)
2	650	16.16	11.59(2)	11.32(3)	6.83(2)	83.6(3)	91.7(2)	88.9(2)	889(4)	0.589(3)
2	188[d]	16.28[d]	11.640(7)	11.137(13)	6.677(9)	82.10(11)	91.38(8)	88.46(8)	857(2)	0.5736(11)

Table 4. Selected angles (°), distances (Å) and polyhedral volumes (Å^3) from the refined structure models of scapolite at different temperatures and pressures, based on the H*P*H*T* data (see text for further details).

Ramp	*T* (°C)	*P* (GPa)	*T*1-*O*1-*T*1	*T*2-*O*2-*T*2	*T*2-*O*3-*T*2	*T*1-*O*4-*T*2	*O*1-*O*4-*O*3	8mR *O*4-*O*4	8mR *O*4-*O*4	8mR ε**	*V*(*M*)***
2	25*	0.0001*	157.8(3)	139.54(4)	146.3(2)	137.1(2)	93.34(9)	3.119(7)	9.335(8)	0.3341(10)	18.82(8)
2	25	1.27	157.7(3)	139.25(4)	146.0(2)	136.6(2)	92.43(9)	3.045(7)	9.323(8)	0.3266(10)	18.34(8)
2	100	1.92	157.5(4)	139.77(7)	146.5(3)	136.3(2)	92.06(10)	3.017(8)	9.313(8)	0.3240(11)	18.27(8)
2	300	4.67	157.6(5)	138.55(6)	145.4(4)	135.3(3)	90.90(13)	2.910(10)	9.290(10)	0.3132(14)	17.41(10)

2	500	6.35	157.6(5)	138.17(6)	144.5(4)	135.3(3)	90.6(2)	2.899(12)	9.275(12)	0.313(2)	17.37(12)
2	650	8.48	158.3(5)	137.8(2)	145.1(3)	135.8(5)	90.20(14)	2.846(12)	9.236(10)	0.308(2)	17.1(2)
2	650	9.41	158.0(5)	137.4(2)	144.6(3)	135.6(5)	90.1(2)	2.84(2)	9.230(12)	0.307(2)	17.0(2)
2	650	10.30	157.5(7)	136.7(3)	145.1(6)	134.1(7)	89.7(3)	2.78(3)	9.28(2)	0.300(3)	16.8(4)

* Sample in the DAC without *P*-medium; ** defined as (8mR *O*4-*O*4 short)/(8mR$_{hk0}$ *O*4-*O*4 long); *** volume of the *M* cation coordination polyhedron calculated using the tools implemented in VESTA3 (Momma and Izumi 2011)

Table 5. Results of the thermal equations-of-state fits to the *V*-*T* data from this study and from literature data (see sections 3.1 and 4.2 for further details).

EoS type	Set of data	Me#	V/V_0 at 25°C	a_0 (x10^5 K^{-1})	a_1 (x10^4 K$^{-1/2}$)	α_V at 25°C (calculated) (x10^5 K^{-1})
*	This study[1]	Me47	0.99986(6)	2.67(8)	-1.06(13)	1.74(3)
*	This study[2]	Me47	0.99990(8)	2.72(10)	-0.98(16)	1.72(4)
**	This study[1]	Me47	1.00022(8)	3.31(3)		1.39(1)
**	This study[2]	Me47	1.00026(8)	3.29(2)		1.39(1)
**	This study[3]	Me47	0.9997(2)	3.42(9)		1.44(4)
**	Baker (1994)	Me23	1.0004(3)	4.59(9)		1.94(4)
**	“	Me35	1.0005(3)	4.08(10)		1.72(4)
**	“	Me60	1.00001(13)	3.55(5)		1.50(2)
**	“	Me90	1.00032(12)	3.12(5)		1.32(2)
**	“	Me100	1.0008(8)	2.91(12)		1.23(5)
**	Graziani and Lucchesi (1982)	Me18	1.0001(6)	4.2(2)		1.79(10)
**	“	Me29	1.0015(5)	4.0(2)		1.68(9)
**	“	Me39	1.0000(4)	3.53(14)		1.49(6)

**	"	Me43	1.0014(5)	3.21(16)	1.36(7)
**	"	Me56	1.0013(5)	2.6(2)	1.09(9)
**	"	Me59	1.0004(4)	2.49(15)	1.05(6)
**	"	Me67	1.0000(4)	2.06(15)	0.87(6)
**	"	Me87	1.0013(4)	1.27(16)	0.54(7)
**	Levien and Papike (1976)	Me33	1.0005(4)	3.65(10)	1.54(4)
**	Antao (2008a)	Me33	0.99984(11)	4.16(4)	1.76(2)
**	Antao (2008b)	Me80	0.99973(11)	3.67(4)	1.55(2)
**	Kabalov (1999)	Me95	0.9980(3)	5.26(11)	2.23(5)

* Eq (1) [see section 3.1]; ** Eq (2) [see section 4.2]; [1] H*T* powder + L*T* single-crystal data; [2] H*T* powder data; [3] H*T* single-crystal data

Figure captions

Figure 1. The crystal structure of scapolite viewed down along [001]. The two independent 4mRs are shown. Independent atomic sites and relevant structural parameters are drawn.

Figure 2. The coordination environment of the *M* site of scapolite (hosting Na or Ca).

Figure 3. (**Upper**) Temperature-dependent evolution of the unit-cell parameters of scapolite (normalized to ambient-conditions values) based on the H*T* powder and L*T* single-crystal data. (**Middle**) Normalized (to ambient conditions values) unit-cell volume of scapolite based on the H*T* powder and L*T* single-crystal data. The black line refers to the refined thermal equation of state (Eq. (1), see section 3.1). (**Bottom**) Thermal expansion coefficients at 25 °C, calculated from refined thermal equations of state (Eq. (2), see section 4.2), *vs.* meionite % for different natural scapolite samples.

Figure 4. Reconstructed reciprocal lattice planes of tetragonal *I*4/*m* scapolite based on the single-crystal H*T* XRD data collected at 25 and 797°C and on the single-crystal L*T* XRD data collected at -100°C.

Figure 5. Temperature-dependent evolution of (**upper**) the inter-tetrahedral *T*-*O*-*T* angles (normalized to ambient conditions values); (**middle**) the *O*1-*O*4-*O*3 angle related to the anti-cooperative rotation of the two independent 4mRs of the scapolite framework; (**bottom**) the interatomic bond distances between the *M* cation (Na or Ca) and the framework oxygens.

Figure 6. (*P*,*T*) phase stability fields of *I*4/*m* and *I*-1 polymorphs of scapolite based on the combined high-pressure and high-temperature XRD data. The very high pressures at which the phase transition has been observed suggest that the triclinic polymorph is very unlikely to appear in a natural geological environment.

This is the peer-reviewed, final accepted version for American Mineralogist, published by the Mineralogical Society of America.
The published version is subject to change. Cite as Authors (Year) Title. American Mineralogist, in press.
DOI: https://doi.org/10.2138/am-2023-8962. http://www.minsocam.org/

Figure 1. The crystal structure of scapolite viewed down [001]. The two independent 4mRs are shown. Independent atomic sites and relevant structural parameters are drawn.

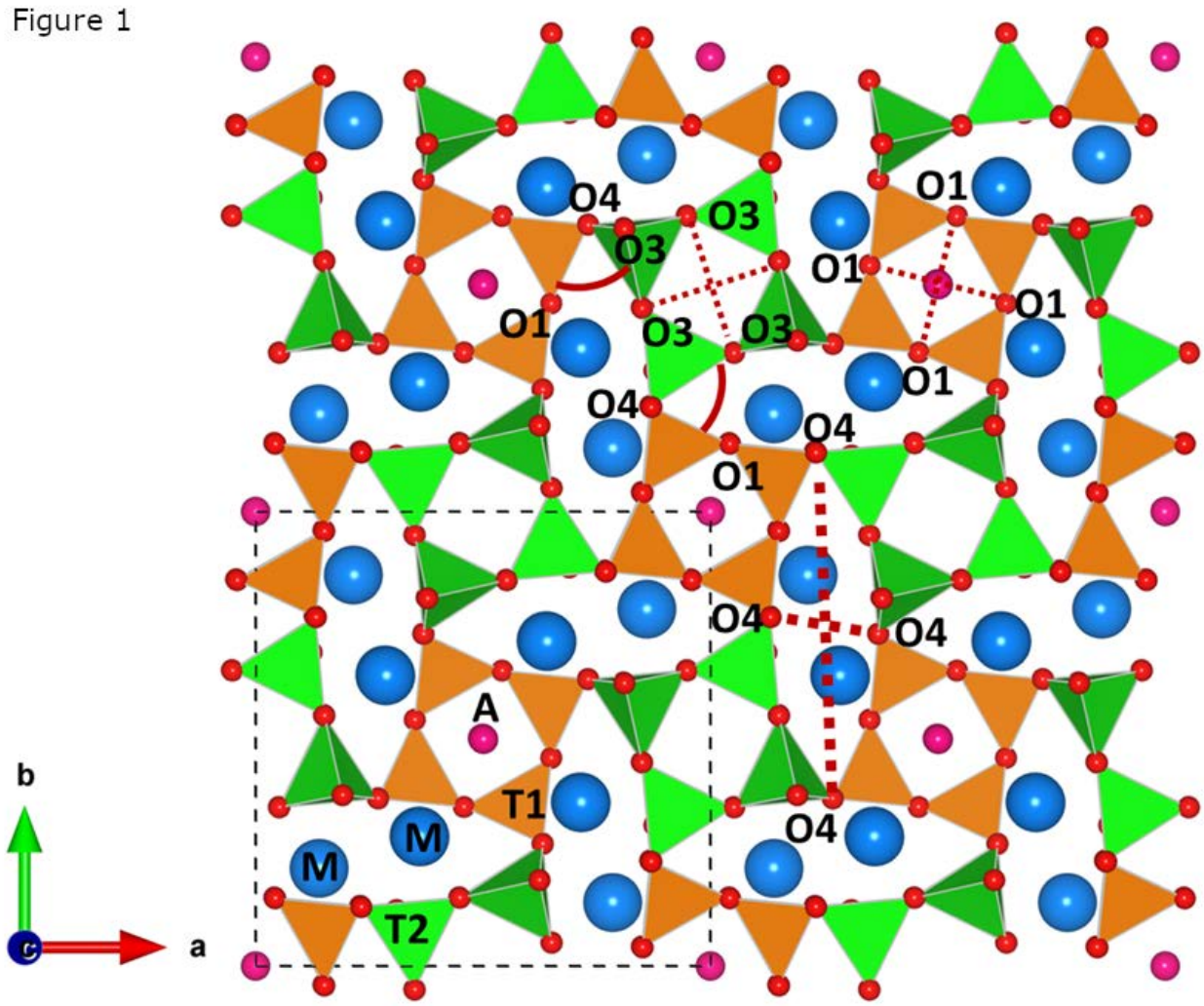

This is the peer-reviewed, final accepted version for American Mineralogist, published by the Mineralogical Society of America.
The published version is subject to change. Cite as Authors (Year) Title. American Mineralogist, in press.
DOI: https://doi.org/10.2138/am-2023-8962. http://www.minsocam.org/

Figure 2. The coordination environment of the *M* site of scapolite (hosting Na or Ca).

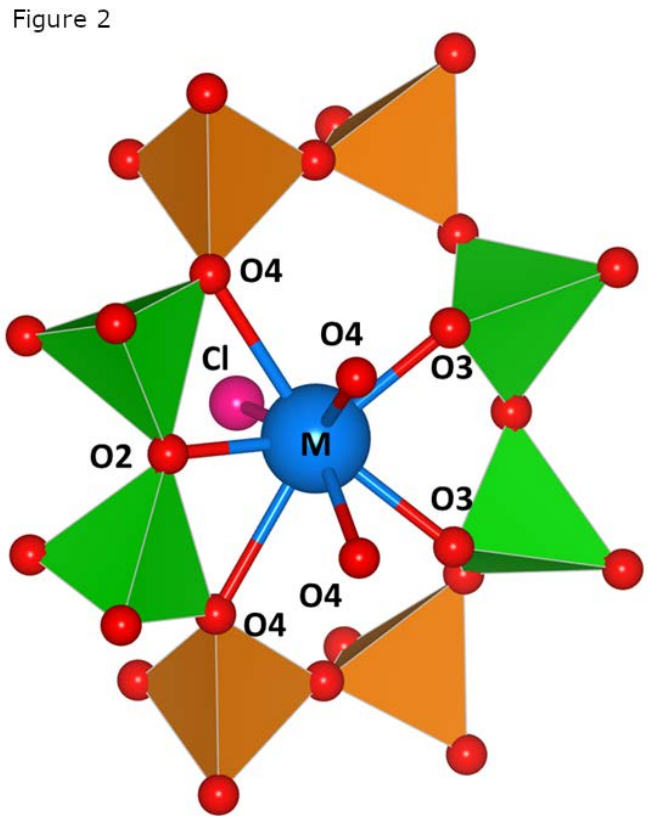

Figure 3. (**Top**) Temperature-dependent evolution of the unit-cell parameters of scapolite (normalized to ambient-conditions values) based on the H*T* powder and L*T* single-crystal data. (**Mid**) Normalized (to ambient conditions values) unit-cell volume of scapolite based on the H*T* powder and L*T* single-crystal data. The black line refers to the refined thermal equation of state (Eq. (1), see section 3.1). (**Bottom**) Thermal expansion coefficients at 25 °C, calculated from refined thermal equations of state (Eq. (2), see section 4.2), *vs.* meionite % for different natural scapolite samples.

This is the peer-reviewed, final accepted version for American Mineralogist, published by the Mineralogical Society of America.
The published version is subject to change. Cite as Authors (Year) Title. American Mineralogist, in press.
DOI: https://doi.org/10.2138/am-2023-8962. http://www.minsocam.org/

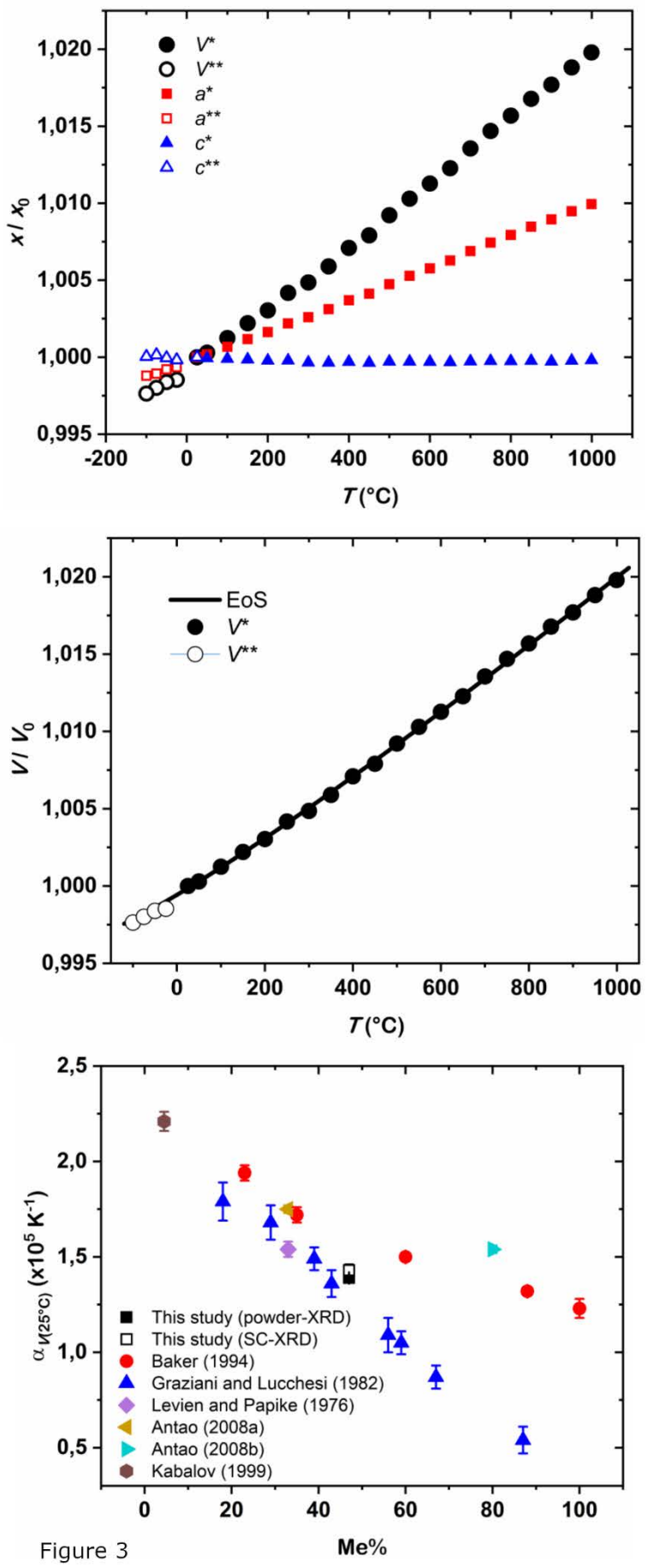

Figure 3

Figure 4. Reconstructed reciprocal lattice planes of tetragonal *I*4/*m* scapolite based on the single-crystal H*T* XRD data collected at 25 and 797°C and on the single-crystal L*T* XRD data collected at -100°C.

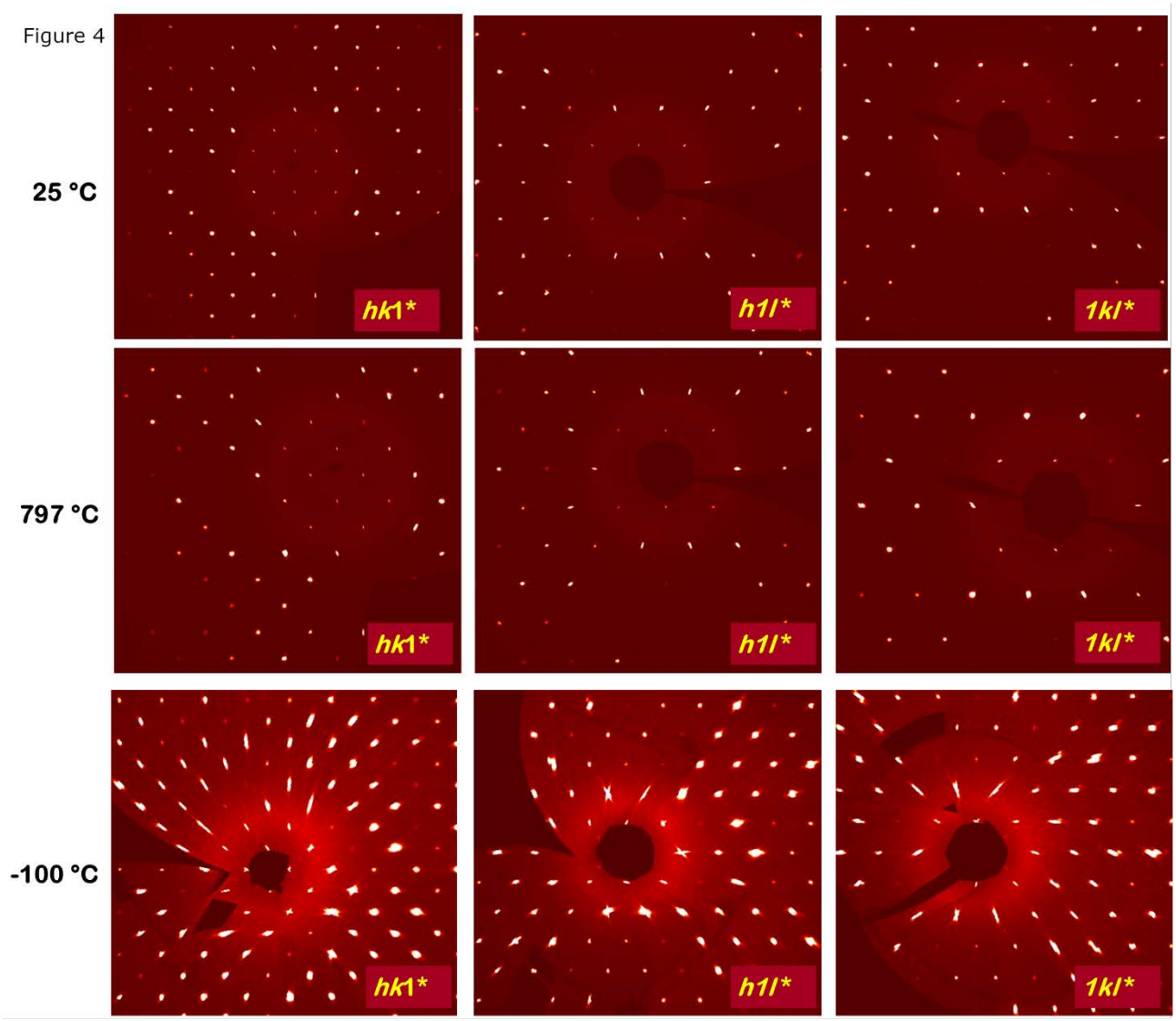

Figure 5. Temperature-dependent evolution of (**top**) the inter-tetrahedral *T*-*O*-*T* angles (normalized to ambient conditions values); (**mid**) the *O*1-*O*4-*O*3 angle related to the anti-cooperative rotation of the two independent 4mRs of the scapolite framework; (**bottom**) the interatomic bond distances between the *M* cation (Na or Ca) and the framework oxygens.

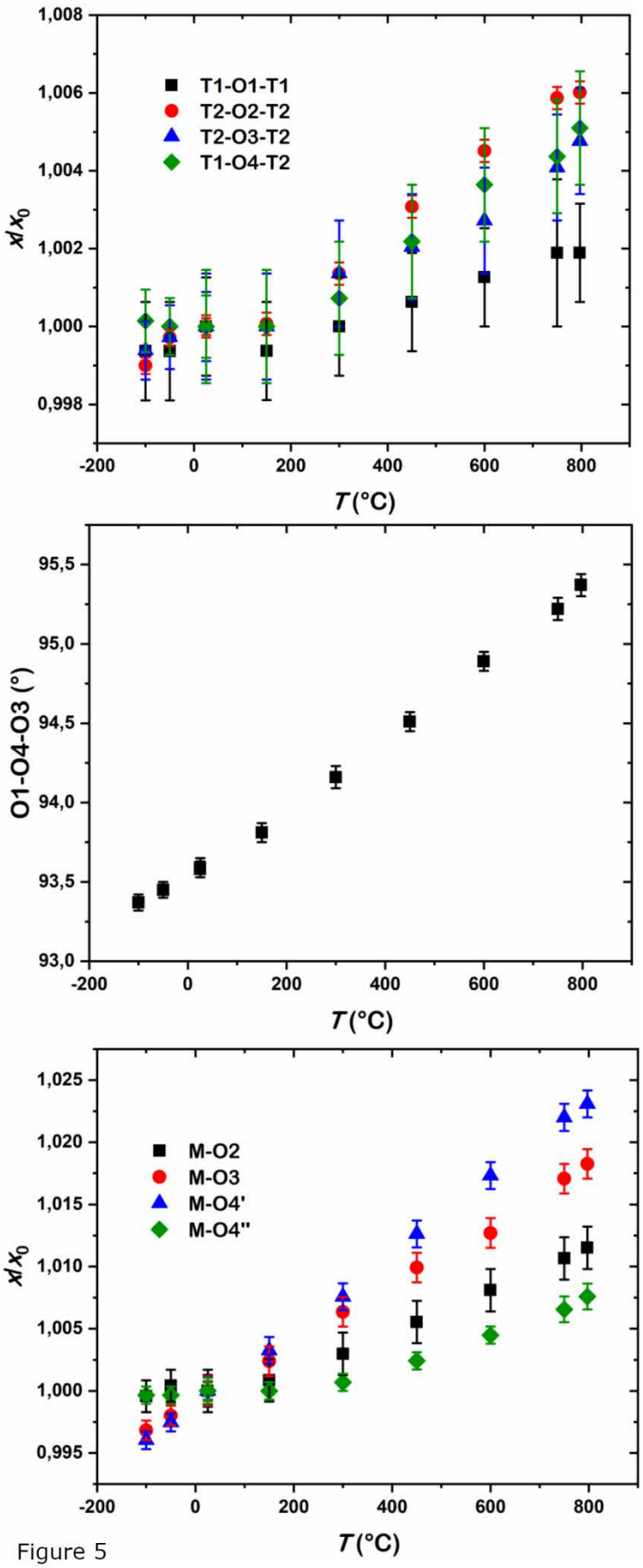

Figure 5

This is the peer-reviewed, final accepted version for American Mineralogist, published by the Mineralogical Society of America.
The published version is subject to change. Cite as Authors (Year) Title. American Mineralogist, in press.
DOI: https://doi.org/10.2138/am-2023-8962. http://www.minsocam.org/

Figure 6. (*P*,*T*) phase stability fields of *I*4/*m* and *I*-1 polymorphs of scapolite based on the combined high-pressure and high-temperature XRD data.

Figure 6